Journal of Aircraft, Available online 12 March 2025
DOI:10.2514/1.c038164

Aerodynamics of High-Bypass-Ratio Aero Engine Nacelles: A Numerical and Experimental Investigation

Fernando Tejero *, David MacManus†, Francisco Sanchez-Moreno ‡, Deneys Schreiner§
Cranfield University, Bedford, United Kingdom, MK43 0AL

Andrea Hill¶
Aircraft Research Association Ltd., Bedford, United Kingdom, MK41 7PF

Christopher Sheaf‖ and Santiago Ramirez-Rubio**
Rolls-Royce plc., P.O. box 31, Derby, United Kingdom, DE24 8BJ

This work presents a numerical and experimental investigation of the nacelle aerodynamics for high bypass ratio aero-engines. A conventional nacelle that is broadly representative of a current standard, and a compact design that is envisaged for future aero-engines, were optimized with an existing computational method. Both nacelles were tested in a large-scale transonic wind tunnel. For the first time, the aerodynamic benefits of compact nacelles are demonstrated through an experimental test campaign. Measurements and CFD simulations confirmed the drag reduction of compact configurations across a wide range of operating points with different flight Mach numbers, massflow capture ratios and angles of attack. For mid-cruise conditions with a Mach number of 0.85, this was a drag reduction of 8.5% and 8.8% for the measurements and the numerical simulations, respectively. These benefits are similar to an isolated optimisation, i.e. not installed in the wind tunnel, which confirmed the capabilities of the design method to identify the drag benefit of compact designs. Relative to the measurements, the main aerodynamic characteristics on the nacelles were captured by CFD in terms of isentropic Mach number distributions and shock location. This work provides a quantitative evaluation for the use of CFD within an industrial setting for nacelle design and analysis.

*Senior Lecturer in Aerodynamic Systems Design, Propulsion Engineering Centre, Cranfield University
†Professor in Propulsion Aerodynamics and Installations, Propulsion Engineering Centre, Cranfield University
‡Visiting Researcher, Propulsion Engineering Centre, Cranfield University
§Research Fellow in Low Emission Propulsion Sytems, Propulsion Engineering Centre, Cranfield University
¶Principal Aerodynamics Engineer, Aircraft Research Association Ltd.
‖Installations Aerodynamics Senior Specialist, Cold Section Aerodynamics, Rolls-Royce plc
**Aerodynamicist, Cold Section Aerodynamics, Rolls-Royce plc

Published by AIAA. This is the Author Accepted Manuscript issued with: Creative Commons Attribution License (CC:BY 4.0).
The final published version (version of record) is available online at DOI:10.2514/1.c038164. Please refer to any applicable publisher terms of use.

Nomenclature

Roman

A	=	Area, $[m^2]$
C_D	=	Nacelle drag coefficient, [-]
D	=	Drag, $[N]$
L	=	Length, $[m]$
M	=	Mach number, [-]
P	=	Pressure, $[Pa]$
q	=	Dynamic head, $[Pa]$
r	=	Radius, $[m]$
Re	=	Reynolds number, [-]
T	=	Temperature, $[K]$
U	=	Uncertainty, [-]

Greek

α	=	Angle of attack, $[deg]$
ϕ	=	Force, $[N]$
ψ	=	Azimuthal location, $[deg]$

Superscripts and Subscripts

0	=	Total conditions
∞	=	Free-stream conditions
bs	=	bounding streamline
hi	=	Highlight
is	=	Isentropic
max	=	Maximum
nac	=	Nacelle
pre	=	Pre-entry
st	=	Static conditions
$sting$	=	Sting
$sting, p$	=	Sting (pressure term)
$sting, v$	=	Sting (viscous term)
te	=	Trailing Edge

Acronyms

ACARE = Advisory Council for Aviation Research and Innovation in Europe

AGARD = Advisory Group for Aerospace Research and Development

ARA = Aircraft Research Association

BC = Boundary Condition

BPR = Bypass Ratio

CFD = Computational Fluid Dynamics

FF = Farfield

HBPR = High Bypass Ratio

MFCR = Mass Flow Capture Ratio

RANS = Reynolds Averaged Navier Stokes

SST = Shear Stress Transport

TWT = Transonic Wind Tunnel

I. Introduction

RELATIVE to year-2000 aircraft, the aerospace performance targets defined by ACARE in Flightpath 2050 aim for a reduction in fuel-burn, landing/take-off NOx emissions, and perceived noise of 75%, 80%, and 65%, respectively [1]. This may be realised through a mix of different technologies such as fuel-efficient and more environmentally friendly turbofan engines [2], sustainable aviation fuels [3], hydrogen powered [4], hybrid [5] or all electric aircraft [6]. Independently of the technology level, the design and optimization of integrated propulsion systems will be a key element in improving efficiency and reducing emissions [7–9] . In this respect, aspects such as the overall sizing, weight, installation and drag of the powerplant can have a significant impact on the overall aerodynamic performance [10]. Within the context of civil aero-engines for podded under-wing configurations, there is a tendency of increasing the bypass ratio (BPR) and reducing the fan pressure ratio to reduce the engine specific fuel consumption and to improve propulsive efficiency [7, 11]. Relative to current in-service architectures that operate at BPR of approximately 10, future turbofans might use bypass ratios above 15 [12]. This large change in engine configuration will require new designs of the intake, nacelle and exhaust system [13, 14]. If traditional design rules are applied, and are simply scaled to accommodate the larger fan diameters, the increase in wetted area and weight may erode the aerodynamic benefits from the low specific thrust cycles. Motivated by these requirements, it is expected that future civil aero-engines will use short and compact housing components [11, 15].

Over the last years, different computational studies have been conducted to understand the aerodynamic feasibility of high bypass ratio (HBPR) aero-engine nacelles. This includes the development of methods to identify the limits of the feasible design space [15], the assessment of nacelle drag trade-off studies between the intake and nacelle [11],

the investigation of the aerodynamic characteristics of compact configurations at off-design conditions [16, 17], and the evaluation of the effect of aircraft integration for these new propulsion systems [9, 18–20]. Tejero *et al.* [15] developed a novel method for the multi-point, multi-objective optimization of compact aero-engine nacelles. As part of the design process, several operating conditions within the cruise segment were considered. The work was based on short configurations in which the ratio of nacelle length (L_{nac}) to highlight radius (r_{hi}) varied from L_{nac}/r_{hi} = 3.0 to 2.4. In addition, the exhaust compactness ranged from a normalised trailing edge (r_{te}) of r_{te}/r_{hi} = 1.0 to 0.89. Across this design space, the nacelle drag varied by approximately 40% which highlighted the large sensitivity of short configurations. The trade-off between intake and nacelle design has been investigated by Peters *et al.* [11]. A range of nacelle lengths were considered, which resulted in changes in the ratio of intake length (L_{int}) to fan diameter (D_{fan}) from L_{int}/D_{fan} = 0.19 to 0.5. Whilst shortening the length had a benefit on nacelle drag, intakes with L_{int}/D_{fan} < 0.25 were unfeasible due to the reduction in fan efficiency. Previous work identified that short nacelles are more sensitive to off-design windmilling conditions, and these operating conditions should be included during the design process [21]. The requirements for multi-point aerodynamic design have been also highlighted by Silva *et al.* [22]. The optimisation process considered crucial conditions of the flight envelope such as mid-cruise, low speed at high angle of attack or crosswind. Relative to a baseline geometry with inlet separation in crosswind conditions, the redesign of the intake and external cowl to avoid boundary layer separation resulted in a 5.1% penalty in nacelle drag at mid-cruise. Similarly, Tao *et al.* [23] also developed a multi-objective optimization capability for short nacelle optimization under different flight conditions. As part of the design process, the nacelle drag at mid-cruise was minimized and the intake pressure recovery at take-off was maximized. The optimization was driven with a multi-fidelity method based on co-kriging, where the low-fidelity and high-fidelity refers to RANS computations with coarse and fine meshes, respectively. Relative to a reference configuration, the mid-cruise nacelle drag was reduced by approximately 23% and the intake pressure recovery was increased by 1.6%. Within the context of novel aircraft concepts and the associated design challenges for airframe-propulsion integration, Yildirim *et al.* [24] developed an adjoint-based method for multi-point optimisation. The work was based on maximising cruise performance subjected to a fan-face distortion constraint at rolling take-off conditions. Relative to a single-point optimisation for mid-cruise conditions, the multi-point approach resulted in a new design with cruise power penalty of around 0.1% but a 37% reduction in fan face distortion at the off-design operating point. Overall, the work highlighted the importance of multi-point optimisation as part of integration design studies. Natural laminar flow nacelles were investigated by Yan *et al.* [25]. The work focused on a conventional 3D non-axisymmetric configuration with $L_{nac}/r_{hi} \approx 3.5$. For transonic conditions with a freestream Mach number of 0.85, it was demonstrated that the nacelle could be redesigned to maintain laminar flow over 30% of the nacelle length. This resulted in a nacelle drag reduction of 5.4% relative to a baseline geometry.

Other key research for compact aero-engine nacelles has been the quantification of the effects of aircraft integration [9, 18–20]. Tejero *et al.* [9] evaluated the changes in the aerodynamic performance of compact and conventional

nacelles for a range of installation positions. It was concluded that, relative to the conventional configuration, there is approximately a 1.2% improvement in the net vehicle force for the compact powerplant when installed in a forward location relative to the wing leading edge. This aligns with the aerodynamic benefits identified for the nacelle in isolation. However, for close-coupled installation positions, the aerodynamic benefit in net vehicle force reduces to 0.44% due to the greater effects of aircraft integration on compact nacelles. The thrust-drag bookkeeping approach was based on the method developed by Goulos *et al.* [18] to calculate the aerodynamic performance of combined airframe-engine architectures. Similar accounting and findings were subsequently reported by Magrini *et al.* [26]. To quantify the aerodynamic effect of the powerplant on the aircraft, Lei *et al.* [27] performed an adjoint optimisation with 462 wing shape variables and 3 engine position variables. Relative to the baseline configuration, the aircraft drag was reduced by 2.7%. Silva *et al.* [19] conducted a comparison of the aerodynamic performance between over-wing and under-wing mounted compact nacelles. For the same aircraft lift coefficient, the over-wing configuration required a greater angle-of-attack compared to the under-wing arrangement. It was highlighted that this has an impact on the nacelle design as its drag increases with the incidence angle. Moreover, it was quantified that for the trimmed condition the overall aircraft drag for the over-wing design was 2% larger than the baseline under-wing arrangement.

There is no open source experimental aerodynamic data for compact HBPR nacelles. Previous wind tunnel tests have been based on relatively long configurations that are not representative of this new design space. The prior experimental work mainly focused on three configurations that were measured at the Aircraft Research Association (ARA) Transonic Wind Tunnel (TWT) [28, 29]. Nacelle-1 was a long nacelle with $L_{nac}/r_{hi} \approx 6.7$ and was designed to assess alternatives to the conventional NACA series 1 type forebody designs [28]. It was axisymmetric with a cylindrical centrebody, a simple circular arc and a conical section for the afterbody. The other two test campaigns for Nacelle-2 and Nacelle-3 were based on nacelles with $L_{nac}/r_{hi} \approx 3.6$. Nacelle-2 was also an axisymmetric configuration without the centrebody section and the conical afterbody. Nacelle-3 was a three-dimensional design with a conventional cylindrical centrebody and a 3D intake with scarf and offset. A summary of the operating conditions for the three TWT tests is provided in Table 1. This experimental data was used by Robinson *et al.* [29] to establish the current state-of-the-art for the validation of RANS CFD methods in nacelle applications. It was concluded that numerical simulations typically predict the nacelle drag within 4% at Mach numbers below the drag rise Mach number. It is important to emphasize that this work was based on nacelles with $L_{nac}/r_{hi} > 3.6$, which are longer than the expected short HBPR aero-engine nacelles with $L_{nac}/r_{hi} \approx 3.0$ [15].

There is a clear need to design compact aero-engine nacelles that will not erode the benefits obtained from the new engine cycles. It is required to determine the possible aerodynamic benefits with respect to conventional configurations. The existing literature is predominantly focused on developing computational methods to design HBPR aero-engine nacelles. The aerodynamic feasibility of these new designs has been claimed following the outcomes of numerical optimizations. However, this has never been confirmed with measurements. Therefore, there is a clear research gap to

Nacelle	Mach number [-]	MFCR [-]	α_{nac} [°]	Re_{rmax} [-]
1	0.4-0.95	0.3-1.0	0	1.5×10^6 - 2.4×10^6
2	0.8-0.89	0.45-0.7	0-4	4.0×10^6
3	0.8-0.88	0.75	4-6	4.0×10^6

Table 1 Summary of flow conditions for previous nacelle experimental data [29]

measure the possible uncertainty of the overall computational design processes. The novelty of this work lies in the demonstration of the aerodynamic benefits of compact nacelles, that are designed and optimized by CFD methods, through wind tunnel testing in an industrial scale transonic facility. The main contribution is that this study provides for the first time a quantitative assessment of the CFD ability to predict the nacelle aerodynamic characteristics of these new configurations. Besides, it validates the optimization system to deliver drag reduction through compact nacelles, and provides a quantitative evaluation for the use of CFD within an industrial setting for design and analysis. In this respect, the numerical uncertainty on the prediction of nacelle drag as well as on the associated flow characteristics are quantified by detailed comparisons with experimental data.

II. Methodology

As part of this work, a nacelle test rig (Section II.A) was recommissioned to undertake state-of-the-art measurements for aero-engine nacelle applications. The experiments mainly involved determining nacelle drag across various operating conditions and mapping pressure distributions along the nacelle to provide insights into the main flow characteristics. Two configurations were designed with an existing multi-point, multi-objective optimization tool [15], and measured in a transonic wind tunnel. One was a long nacelle with a conventional $L_{nac}/r_{hi} = 3.6$. This was established to benchmark the aerodynamic benefits of the second optimized configuration that is representative of an HBPR design with a short $L_{nac}/r_{hi} = 3.1$ [9, 18]. Computational analyses were carried out for the rig arrangement to validate the CFD approach that is usually used within an industrial design setting (Section II.B).

A. Experimental approach

The high speed wind tunnel measurements were performed using the ARA large scale nacelle test rig (Figure 1). This rig was installed in the ARA 8' × 9' (2.4m × 2.7m) transonic wind-tunnel (TWT). The nacelle drag was determined with a wake momentum survey and derived from pressure measurements (Figure 1). Overall, five traversing pressure rake arms with 29 total pressure Pitot heads and 7 static pressure radial measurement positions were used in each arm. The location of the Pitot heads was biased towards the nacelle support sting to enhance the resolution in the boundary layer (Figure 1). The rake arm was rotated to provide a total of 15 azimuthal positions, which equates to 24° resolution. This ensures that non-axisymmetric flow features induced by the nacelles can be measured. The nacelle and sting

were instrumented with static pressure tappings to provide detailed measurements of the nacelle flow characteristics as well as to enable drag corrections due to the additional viscous drag terms generated on the sting [30]. Five azimuthal locations around the nacelle surface were instrumented at $\psi = 0°$, 45°, 90°, 135° and 180° with 30, 26, 27, 18 and 22 axially-distributed static pressure taps, respectively. The sting was instrumented at the aero-lines of $\psi = 0°$, 90° and 180° with 17 axially-distributed taps each. It is important to note that the sting begins with a contraction just after the nacelle's trailing edge. This was designed to mimic the initial streamtube of an equivalent isolated aero-engine nacelle. As a result, the pressure distribution on the nacelle afterbody and the initial contraction is similar to the isolated case. The sting's shape was defined for mid-cruise conditions and remained unchanged throughout all measured operating points. This approach represents an improvement over previous nacelle wind tunnel campaigns, where the sting had a cylindrical shape [28], which is less accurate in representing post-exit forces.

A wide range of operating conditions were evaluated. Although the main focus was on mid-cruise, the sensitivities to the key aerodynamic parameters of freestream Mach number (M), massflow capture ratio (MFCR) and angle of attack (α_{nac}) were also investigated. The massflow capture ratio (MFCR in Eq. 1) is a function of massflow through the intake (m_{intake}), the nacelle highlight area (A_{hi}) and the free-stream density (ρ) and velocity (V). An overview of the operating conditions is presented in Section III.B. The freestream Mach number was derived from the measured total and static pressures in the settling chamber and working section plenum chamber, respectively. The uncertainty on the static and total pressures takes into account the measurement system calibration which includes error contributions due to transducer non-linearity, hysteresis and non-repeatability [31, 32]. Bias and random uncertainty contributions were combined by summation and quadrature using an Euclidean norm and assessed at the 2σ level. The overall uncertainty on the wind tunnel Mach number and isentropic Mach number was up to about ±0.002. The intake massflow was controlled with a valve located between the rig and the suction source. It was measured using an in-line venturi installed upstream of the throttle valve. The venturi was calibrated against an industrial standard airmeter [33]. Including the terms from the calibration and the venture pressure measurements, the overall uncertainty on MFCR was ±00.004 at the nominal cruise point and up to ±0.01 across the range of operating conditions. Nacelle incidence was set by means of a turntable in the floor of the TWT working section (Figure 1). The overall uncertainty on incidence was 0.05° which included the model support deflection, the port to starboard sidewash angle in the working section, and the stochastic uncertainty in the turntable setting angle. Nacelle drag was determined from the wake rake survey and the uncertainty assessment included the static and total pressure terms outlined above. For both nacelle configurations at mid cruise, bias and random contributions were of order +0.5% and ±0.9%.

$$MFCR = \frac{m_{intake}}{\rho V A_{hi}} \tag{1}$$

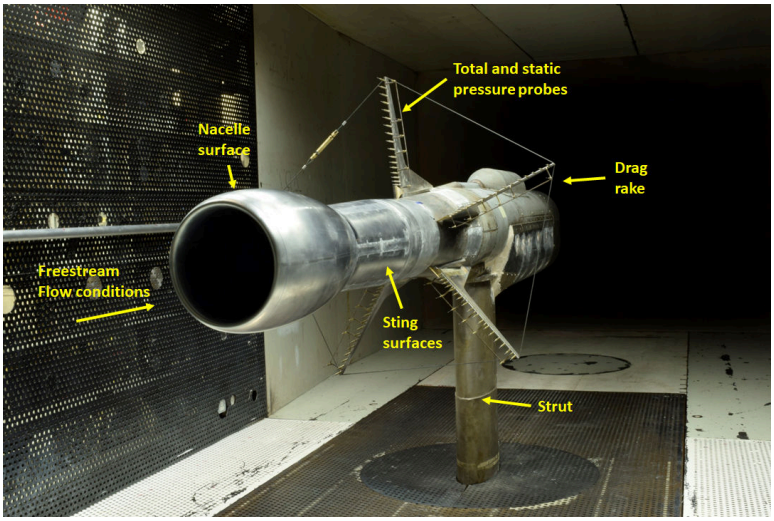


Fig. 1 Front view of the ARA Z30 large scale nacelle test rig

B. Numerical approach

1. Nacelle design and optimization

The nacelle optimization process was based on a well-established numerical method developed by Tejero *et al.* [15], which has been successfully used in the past to evaluate the aerodynamic feasibility of compact aero-engine nacelles. A thorough description of the method has been provided in previous work and, therefore, only a brief description is presented here. The shapes of the aero-engine nacelles are parametrized with the intuitive class shape transformation method [15]. The azimuthal definition is controlled with 5 aero-lines ($\psi = 0°$, $45°$, $90°$, $135°$ and $180°$), and overall a total of 20 geometric degrees of freedom are used during the optimization process. The geometry definition includes the intake requirements of droop and scarf angle [11]. The computational approach is based on solving the Favre-averaged Navier–Stokes equations with the $k - \omega$ SST turbulence model. During the optimization process a range of flight conditions are considered. This includes operating points within the cruise segment as well as off-design windmilling to ensure the aerodynamic robustness of the designs [21]. The nacelle drag is extracted with the AGARD thrust-drag bookkeeping method [34]. The multi-point, multi-objective optimization is carried out with the Non-Dominated Sorting Genetic Algorithm II (NSGA-II) gradient-free algorithm [35]. The design process was based on an isolated arrangement [15], without the different elements of the wind tunnel, e.g. sting or strut.

2. Computational approach for the rig arrangement

Although the nacelles were optimized as an isolated configuration (Section II.B.1), the wind tunnel tests used an established sting mounted arrangement (Figure 1). Therefore, for the assessments of the wind tunnel configuration a consistent CFD method was adopted. The viscous and compressible steady Favre-averaged Navier-Stokes equations are solved in Ansys Fluent [36] with a double precision, density-based and implicit approach. This works uses the

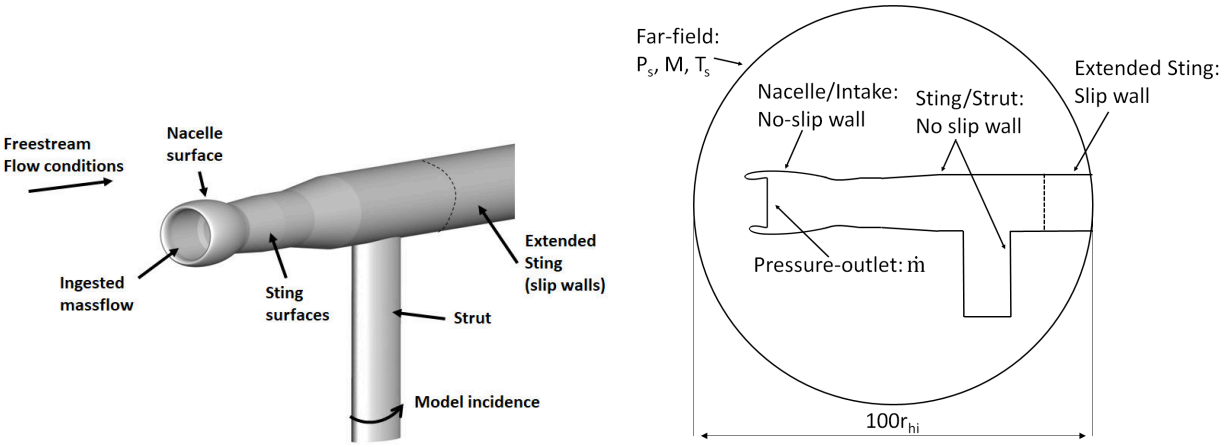
$k-\omega$ SST turbulence model. The Green-Gauss node-based method for the flow-field gradients was used with a second-order accurate upwind scheme. The dynamic viscosity is calculated with Sutherland's law [37] and the thermal conductivity with kinetic theory. This is the same numerical method as the used for the isolated nacelle design and optimization (Section II.B.1). The nacelle boundary layer was tripped using discrete roughness elements which were placed approximately at 5% of the nacelle chord from the leading edge. The successful transition to fully turbulent flow was proven using acenaphthene visualisation. The CFD simulations assumed fully turbulence flow. A far-field type Boundary Condition (BC) was used to avoid the complexity of modeling the TWT wall porosity [17]. A spherical domain was used with a diameter of 100 $\times r_{hi}$, where r_{hi} refers to the nacelle highlight radius. The spherical boundary was defined with a pressure far-field in which the Mach number (M), and static pressure (P_s) and temperature (T_s) are imposed to match the operating conditions of the TWT. The intake massflow was controlled with a static pressure BC to meet the required operating conditions. The intake, nacelle, sting and strut surfaces were modelled as adiabatic and viscous no-slip walls (Figure 2b). The sting surface that was extended to the farfield was modelled with a slip wall condition. A hybrid mesh was used with structured prism layers near the walls and tetrahedral elements in the remainder of the domain. The first cell height was adjusted to satisfy a y^+ of 1 for the no-slip walls. Mesh refinement zones were added in the nacelle highlight and its body vicinity to capture the flow gradients and shock waves. The spatial discretisation was based on a grid sensitivity study [38]. Overall, three different meshes with 4.4 $\times 10^6$, 15.9 $\times 10^6$ and 46.2 $\times 10^6$ cells were considered. For typical mid-cruise conditions with M = 0.85, MFCR = 0.7 and α_{nac} = 4.5°, the grid convergence index of the medium mesh with 15.9 $\times 10^6$ elements was 1.0% based on nacelle drag. This is similar to the uncertainty of the measurements, and this grid was used for the investigation. The pressure outlet boundary condition used a uniform static pressure. Whilst no experimental data was recorded to verify this assumption, a CFD study assessed its impact on nacelle drag and isentropic Mach number along the nacelle. The difference in nacelle drag between a reflective and non-reflective pressure-outlet condition was in the order of 0.01%. This is almost two orders of magnitude lower than the experimental uncertainty. In addition, the changes in the isentropic Mach number distribution on the nacelle were negligible.

C. Thrust-drag bookkeeping for the rig arrangement

The nacelle drag in the wind tunnel configuration ($D_{nac,TWT}$ in Eq. 2) is defined as the sum of the pre-entry streamtube force (ϕ_{pre}), the pressure and viscous terms of the force exerted on the nacelle surface from the stagnation point to the trailing edge (ϕ_{nac}) and the pressure component on the sting up to the rake location ($\phi_{sting,p}$) (Figure 3).

$$\mathrm{D_{nac,TWT}} = \phi_{\mathrm{pre}} + \phi_{\mathrm{nac}} + \phi_{sting,p} \tag{2}$$

in which the term ϕ in the drag axis is expressed as in Eq. 3:



(a) Overview **(b) Boundary conditions (not to scale)**

Fig. 2 Computational model of the ARA Z30 nacelle test rig

$$\phi = \int_S (p_s - p_\infty)\, \overrightarrow{e_D} \cdot \overrightarrow{dS} + \int_A \tau \overrightarrow{e_D} \cdot \overrightarrow{dA} \tag{3}$$

where p_s is the local static pressure, p_∞ refers to the static pressure at infinity, τ is the wall shear stress, $\overrightarrow{e_D}$ is the unit vector in drag direction and the terms $\overrightarrow{dS}$ and $\overrightarrow{dA}$ refer to the surface normal and tangential unit vectors, respectively.

As described above, the force acting on the nacelle surface comprises viscous and pressure terms. The viscous component is mainly dominated by the nacelle wetted area and the boundary layer characteristics. The pressure term is related to the pressure distribution along the nacelle and the projection of the nacelle area in the drag axis. For transonic conditions, there is usually a shock wave which results in shock losses and wave drag. As such, the associated lift distribution has a large impact on the nacelle drag. The pre-entry term (ϕ_{pre}) is dictated by the MFCR. For example, it increases as MFCR reduces. However, this also affects the forces on the nacelle surface. For a reduction of MFCR, the pressure force reduces around the nacelle lip which is beneficial for the overall nacelle drag. However, it also results in a stronger pre-shock Mach number, and a concomitant larger wave drag. Therefore, there is a trade-off between the initial acceleration and the shock strength. For the wind-tunnel arrangement, the sting post-exist force is linked to the static pressure at the nacelle trailing edge. Within a broader context, it is important to highlight that for isolated arrangements with an exhaust system, the post-exit force is also a function of the exhaust pressure ratio.

The nacelle drag was calculated with a wake integration method. The mathematical derivation of the accounting is provided below.

A control volume (CV in Figure 3) can be defined, which encloses the upper streamline (ϕ_{bs}), and the contributions on the lower side of ϕ_{pre}, ϕ_{nac} and ϕ_{sting} (Figure 3). These terms can be related to the gauge forces (F_G) at sections 3 and 00 through a momentum balance (Eq.4):

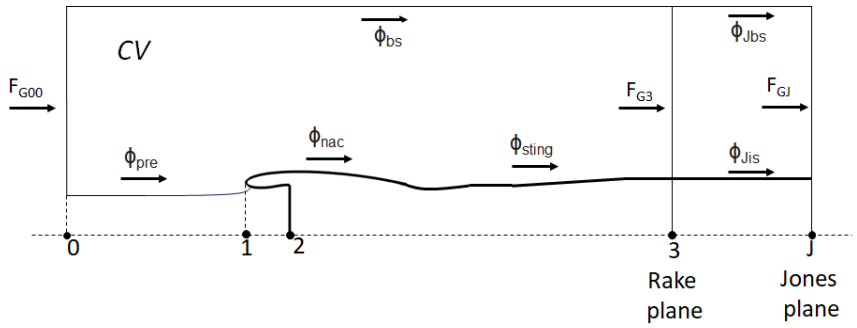


Fig. 3 Schematic of the thrust-drag bookkeeping method

$$-F_{G00} + \phi_{bs} + F_{G3} + \phi_{pre} + \phi_{nac} + \phi_{sting} = 0 \tag{4}$$

where the gauge force (F_G) in the drag axis is defined as in Eq. 5:

$$F_G = \int_S (p - p_\infty)\, \overrightarrow{e_D} \cdot \overrightarrow{dS} + \int_S (\rho |\vec{U}| \vec{U}) \overrightarrow{e_D} \cdot \overrightarrow{dS} \tag{5}$$

and ρ is the density and $\vec{U}$ is the velocity vector.

The force acting on the sting up to the rake location, i.e. ϕ_{sting}, encompasses both pressure and viscous terms. Therefore, Eq. 4 can be rewritten to Eq. 6:

$$-F_{G00} + \phi_{bs} + F_{G3} + \phi_{pre} + \phi_{nac} + \phi_{sting,p} + \phi_{sting,v} = 0 \tag{6}$$

where $\phi_{sting,p}$ and $\phi_{sting,v}$ are the pressure and viscous terms acting on the sting, respectively.

Within the context of nacelle drag in the wind tunnel sting mounted configuration, the sting viscous term is a spurious contribution, and its magnitude is primarily influenced by the location of the rake plane. Therefore, this term is excluded in the drag accounting. This is consistent with isolated nacelle configurations, i.e. not installed in the wind tunnel, where only the pressure term on the post-exist streamtube is accounted for.

The combination of Eq. 2 and 6 results in the definition of nacelle drag in the wind tunnel (Eq. 7):

$$D_{nac,TWT} = F_{G00} - F_{G3} - \phi_{bs} - \phi_{sting,v} \tag{7}$$

It is important to note that the total pressure at the rake plane (Station 3 in Figure 3) is used to calculate the momentum deficit from the freestream conditions with the Jones' method [39]. For this purpose, the flow variables are isentropically expanded to the Jones plane (Station J in Figure 3). The expansion assumes constant massflow, total temperature, total pressure and expands to the free-stream static conditions. The expansion to the Jones plane is performed due to the

sparse static pressure measurements in the rake plane, which are limited to 7 radial locations. Although the static pressure could have been interpolated to match the radial locations of the total pressure measurements, allowing for the calculation of the velocity as part of the gross force definition (F_{G3}), the Jones plane approach is applied in this work because it is a well-established method in wind tunnel testing and has been successfully used in previous studies [28, 40, 41]. Due to this expansion, two additional terms are added in the thrust-drag bookkeeping accounting: ϕ_{Jbs} and ϕ_{Jis} (Figure 3). Therefore, the nacelle drag can be also expressed as in Eq. 8:

$$\mathrm{D_{nac,TWT}} = \mathrm{F_{G00}} - \mathrm{F_{GJ}} - \phi_{\mathrm{bs}} - \phi_{sting,v} - \phi_{\mathrm{Jbs}} - \phi_{\mathrm{Jis}} \tag{8}$$

The nacelle drag requires all the terms presented in Eq. 8. Due to the isentropic expansion to the Jones plane, the term of ϕ_{Jis} is zero. The forces on the bounding streamlines, i.e. ϕ_{bs} and ϕ_{Jbs} cannot be measured in the experiments. As such, a modified nacelle drag ($\mathrm{D^{mod}_{nac,TWT}}$ in Eq. 9) is defined, and used in this work. Whilst this formulation neglects the influence of the terms ϕ_{bs} and ϕ_{Jbs}, the values are several order of magnitude smaller than the infinity gauge force term, i.e. F_{G00}. The magnitude was quantified with CFD. For typical mid-cruise conditions with M = 0.85, MFCR = 0.7 and $\alpha_{nac} = 4.5°$, the values of ϕ_{bs} and ϕ_{Jbs} were 0.02% and 0.1% relative to F_{G00}, respectively. For consistency, the experimental and numerical results are reported with the same nacelle drag formulation (Eq. 9).

$$\mathrm{D^{mod}_{nac,TWT}} = \mathrm{F_{G00}} - \mathrm{F_{GJ}} - \phi_{sting,v} \tag{9}$$

For the experimental data, the term $\phi_{sting,v}$ is determined using the Green's method [30]. However, for the numerical results the Green's tool is not applicable and $\phi_{sting,v}$ is extracted directly from the CFD solution. To calculate F_{GJ}, the CFD data was interrogated with the same radial and azimuthal resolution as the rakes to provide a direct comparison between measurements and CFD.

The nacelle drag coefficient (Eq. 10) is obtained by normalising the modified nacelle drag (Eq. 9) with the dynamic head and the nacelle highlight area (A_{hi}).

$$\mathrm{C_D} = \frac{\mathrm{D^{mod}_{nac,TWT}}}{\frac{1}{2}\rho_\infty \mathrm{V_\infty^2 A_{hi}}} \tag{10}$$

The gauge forces of F_{G00} and F_{GJ} were calculated with the data from the rake plane (Section 3). Whilst the derivation below is for the experiments, the same approach was followed for the CFD results. For each probe, the pressure ratio (PR_J in Eq. 11) at the Jones plane was calculated as the ratio between the measured total pressure ($P_{0,\mathrm{rake}}$) at the rake plane and the measured static pressure in the settling chamber ($P_{s,\mathrm{WT}}$).

$$PR_J = \frac{P_{0,\mathrm{rake}}}{P_{s,\mathrm{WT}}} \tag{11}$$

This ratio was then used to derive the associated Mach number (M_J in Eq. 12) by applying isentropic relation for compressible flow:

$$M_J = \sqrt{\frac{2}{\gamma - 1}\left[(PR_J)^{\frac{\gamma-1}{\gamma}} - 1\right]} \tag{12}$$

where γ is the specific heat ratio, and was set to 1.4.

Similarly, the static temperature in each rake location at the Jones plane ($T_{s,J}$ in Eq. 13) was obtained by:

$$T_{s,J} = \frac{T_0}{1 + \frac{\gamma-1}{2}M^2} \tag{13}$$

where T_0 is the total temperature at the working section.

The velocity in each probe (V_J) was calculated with Eq. 14:

$$V_J = M_J \cdot \sqrt{\gamma \cdot R \cdot T_{s,J}} \tag{14}$$

where R is the specific gas constant for air.

Then, the gauge force at the Jones plane (F_{GJ}) was calculated with an area-weighted of $m_3 \times V_J$, where m_3 was estimated from the static pressure measurements at the rake plane. In addition, the term F_{G00} was defined as $m_3 \times V$, where V is the measured velocity at the settling chamber.

III. Results and analysis

A. Isolated nacelle design and optimization

Two independent multi-point, multi-objective optimizations (MOO) were performed with the methodology described in Section II.B.1. These were for a conventional nacelle with a $L_{nac}/r_{hi} = 3.6$ and a compact configuration with $L_{nac}/r_{hi} = 3.1$. A set of conditions that include mid-cruise and 3 different off-design windmilling scenarios were considered (Table 2). The estimation of MFCR values for windmilling was based on the ESDU method [42]. It is acknowledged that this approach may yield lower MFCR values than those anticipated for ultra-high bypass ratio aero-engines. Therefore, the operating conditions considered in this study are based on a conservative scenario, and a more challenging aerodynamic design space. As part of the optimization process, regression functions were used, in which the nacelle drag was minimised (Table 2). For each design, Pareto fronts were generated as part of the MOOs, and one nacelle from each optimization was downselected [15]. For mid-cruise condition with $M = 0.85$, MFCR = 0.7 and $\alpha_{nac} = 4.5°$, the nacelle drag for the compact design was 8.7% lower than the conventional configuration.

To provide an overview of the aerodynamics of both downselected nacelles, the isentropic Mach number (M_{is}) distribution at mid-cruise (Table 2) is presented in Figure 4. Both configurations have a stronger initial acceleration

Name	Mach number [-]	MFCR [-]	α_{nac} [°]
Mid-cruise	0.85	0.7	4.5
Windmilling Diversion	0.65	0.33	4.5
Windmilling End-of-Runway	0.20	0.32	20
Windmilling Engine-out	0.85	0.35	4.5

Table 2 Operating conditions for the multi-point, multi-objective optimization

around the nacelle lip at the top (ψ = 0°) and top-control (ϕ = 45°) aero-lines than for the other controlled ones (ψ = 90°, 135° and 180°). This is caused by changes in the location of the stagnation point as well as the initial radius of curvature as a function of the azimuthal position. For a nacelle at incidence and MFCR<1, the stagnation point will be located inside the intake at the top aero-line. This results in a large acceleration of the flow due to its turning around the lip. The stagnation point moves within the intake towards the lip as the azimuthal location increases. For the azimuthal locations of ψ = 135° and 180°, the stagnation point is located on the outer nacelle aero-line, and therefore, there is a reduction in the initial flow acceleration. For both nacelles, the initial radius of curvature decreases with azimuthal location. The combination of both mechanisms makes that the top and top-control aero-lines have larger peak isentropic Mach numbers. For all the azimuthal positions, the compact nacelle has a greater peak M_{is} than the conventional one. The largest difference arises at ψ = 45° with a ΔM_{is} = 0.07 (Figure 4). This reduces to approximately ΔM_{is} = 0.02 at the top aero-line, i.e. ψ = 0°. For these two aero-lines of the top-quadrant (ψ = 0° and 45°), the shock location is similar between the compact and conventional architectures with a small difference of $\Delta X/L_{nac}$ = 0.01. For the bottom quadrant, the nacelle aerodynamics are generally benign in both configurations with low peak and pre-shock isentropic Mach numbers (Figure 4). Therefore, relative to the aero-lines ψ = 0° and 45°, the contribution of the bottom quadrant to the overall nacelle drag is less. It is worth noting that the greatest aerodynamic changes between the L_{nac}/r_{hi} = 3.1 and 3.6 architectures arise at ψ = 45°, which has the largest impact on the drag reduction of the compact nacelle.

Figure 5 presents the side aero-line (ψ = 90°) of both downselected nacelles. In the compact configuration, the shortened length results in a reduced maximum nacelle radius and a smaller initial radius of curvature. It showcases the required geometrical modifications for this design space relative to conventional architectures.

B. Overview of the experimental test campaign

The main objective of this research is to demonstrate that the aerodynamic benefits identified during the numerical optimizations (Section III.A) are also met experimentally. The coverage of the measurements in the M-MFCR space is presented in Figure 6. For all the operating points, two angles of attack that are expected for typical mid-cruise conditions were measured: α_{nac} = 3.0° and 4.5°. Within the available experimental budget, approximately 70% of the experimental data was generated for the compact nacelle (L_{nac}/r_{hi} = 3.1). (Figure 6). This was to fully characterize the

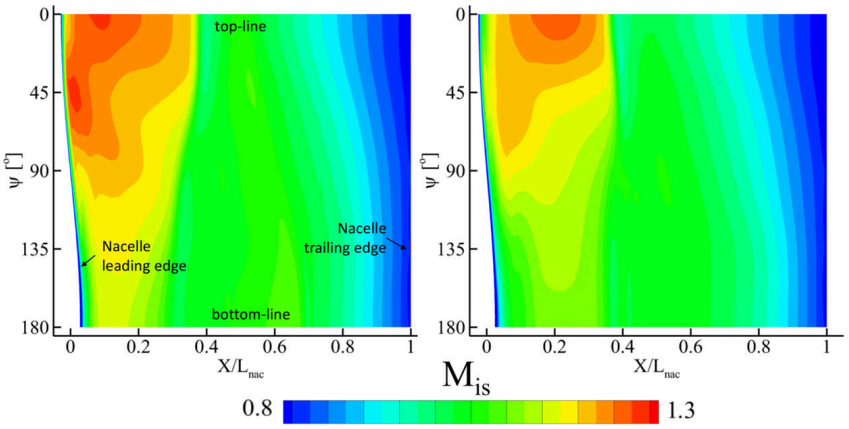


Fig. 4 Computed unwrapped surfaces of the nacelle: Compact configuration (left) and conventional configuration (right)

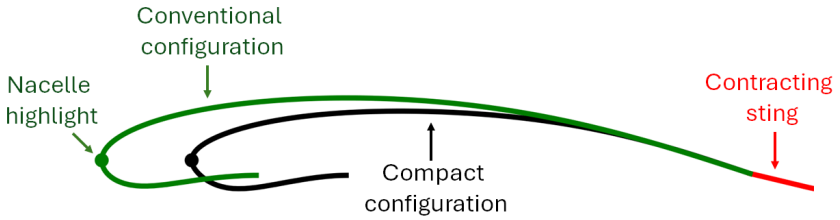


Fig. 5 Comparison of the side aero-line ($\psi = 90°$) of both downselected nacelles. The initial shape of the sting for the wind-tunnel arrangement is also presented for reference

associated nacelle aerodynamics for future civil aero-engine nacelles, which is crucial for a better understanding of this design space.

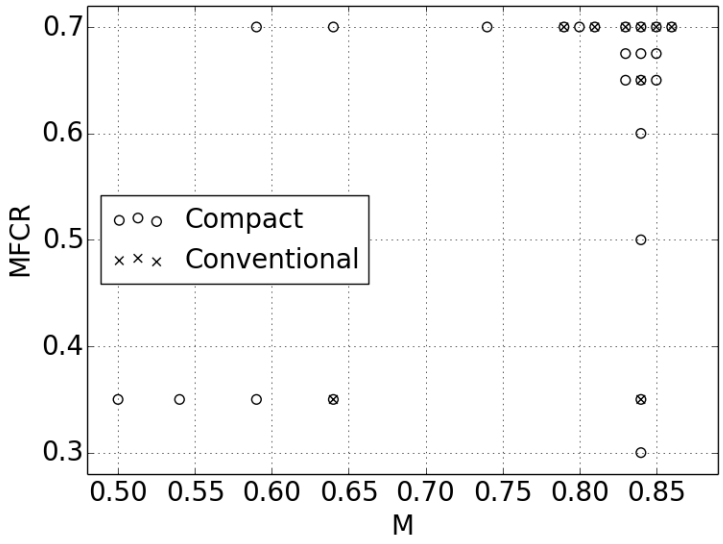


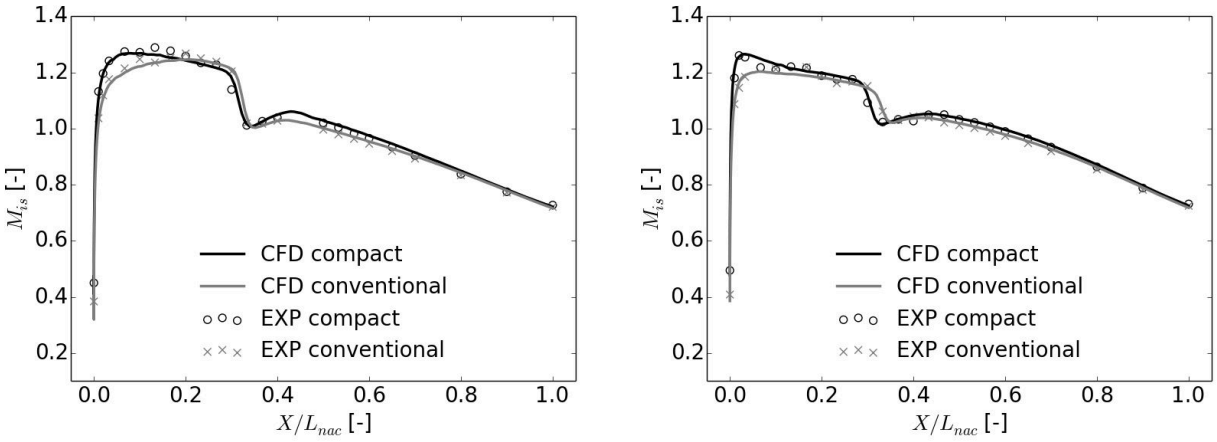
Fig. 6 Conditions measured during the transonic wind tunnel testing in the M-MFCR space. All points were evaluated at $\alpha_{nac} = 3.0°$ and $4.5°$

C. Nacelle aerodynamic characteristics: rig arrangement

1. Mid-cruise conditions

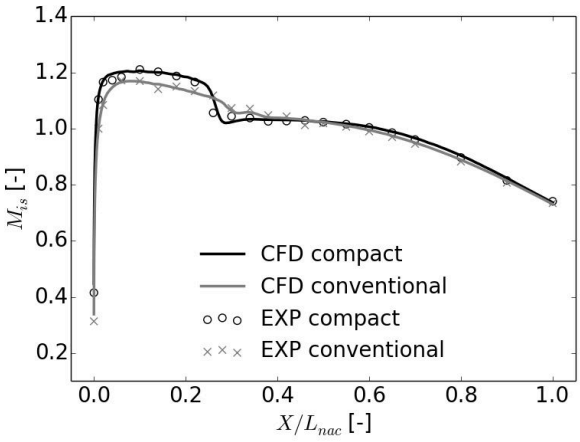
To provide an initial insight of the experimental and numerical flow aerodynamics of the installed nacelle in the rig, the nominal mid-cruse condition with M = 0.85, MFCR = 0.7 and $\alpha_{nac} = 4.5°$ is considered. Figure 7 shows the isentropic Mach number distributions in all the 5 controlled aero-lines for the compact and conventional nacelles. For both designs, and across the different azimuthal locations ($\psi = 0°, 45°, 90°, 135°$ and 180°), the agreement between the measurements and CFD is excellent. The numerical results accurately predict the main flow characteristics of peak M_{is}, pre-shock M_{is} and shock location. For both nacelles, the difference between CFD and measurements in terms of peak and pre-shock isentropic Mach number is within $\Delta M_{is} \approx 0.003$. In addition, the maximum shock location difference is $\Delta X/L_{nac} \approx 0.05$, which is similar to the spatial resolution of the experimental static pressure tappings. This isentropic Mach number distributions are traditional for transonic external aerodynamics, which are characterised by an initial acceleration around the leading edge, a normal shock wave and a continuous flow deceleration towards the trailing edge [22, 43]

The boundary layer at the downstream rake location (Figure 1) was measured in a total of 15 azimuthal rake positions (Section II.A). Figure 8 compares the experimental and computational normalised total pressure at the rake location. The larger momentum deficit appears in the azimuthal locations between $\psi = 0°$ and 96°. As presented in Figure 7, the most challenging transonic flow aerodynamics are on the top quadrant ($\psi = 0°, 45°$ and 90°) where the peak and pre-shock isentropic Mach number are the greatest. Therefore, this aero-lines have the largest momentum deficit within the boundary layer caused by shock-wave boundary layer interaction and the larger wave drag and losses. The experimental data reveals a larger deficit in the aero-lines of +24° and -24° relative to 0°, which is also captured by the CFD simulations. Figure 9 shows a subset of the measured boundary layer profile for the azimuthal locations of $\psi = 0°, 48°$ and 96°. These are the closest positions to the design controlled aero-lines of $\psi = 0°, 45°$ and 90° with the available experimental rake resolution of 24°. Overall, there is good agreement between the CFD and the measurements. The simulations successfully predict the reduction in momentum deficit as the azimuthal location (ψ) increases. This can be observed by comparing the boundary layer thickness, which reduces by approximately 50% from $\psi = 0°$ to 96°. Both, numerical and experimental results, show that the boundary layer profiles for the compact and conventional designs are similar for the azimuthal locations of $\psi = 0°$ and 96°. Therefore, at these locations the contribution to the changes in the overall nacelle drag between both configurations is low. The main differences appear at $\psi = 48°$, where there is a larger momentum deficit within the boundary layer for the conventional nacelle relative to the compact one. This azimuth has the largest impact on the nacelle drag changes between configurations. For the lower nacelle quadrant, the agreement between CFD and measurements is similar to those shown in Figure 9 and, therefore, it is not presented here.

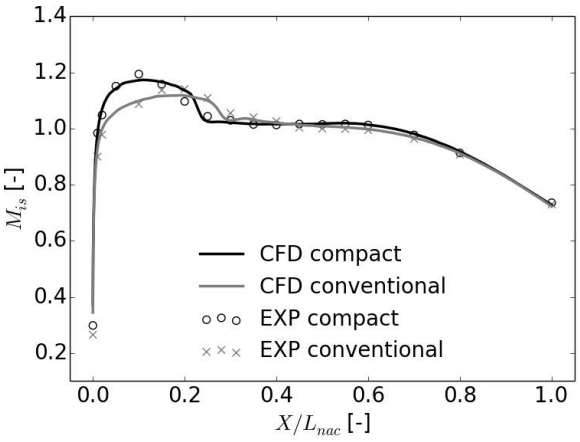


(a) $\psi = 0°$

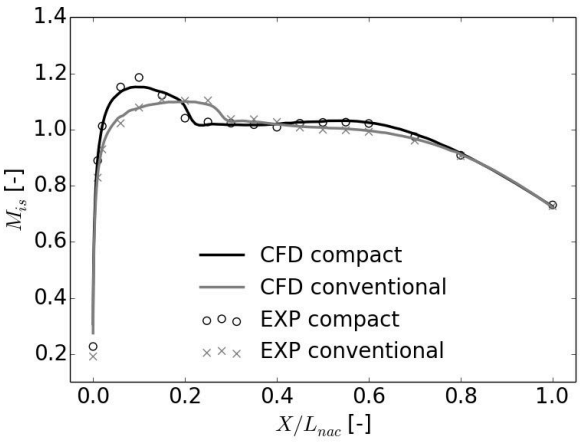
(b) $\psi = 45°$



(c) $\psi = 90°$



(d) $\psi = 135°$



(e) $\psi = 180°$

Fig. 7 Isentropic Mach number distribution along the compact nacelle (L_{nac}/r_{hi} = 3.1) and conventional nacelle (L_{nac}/r_{hi} = 3.6) at mid-cruise conditions (M = 0.85, MFCR = 0.7 and $\alpha_{nac} = 4.5°$)

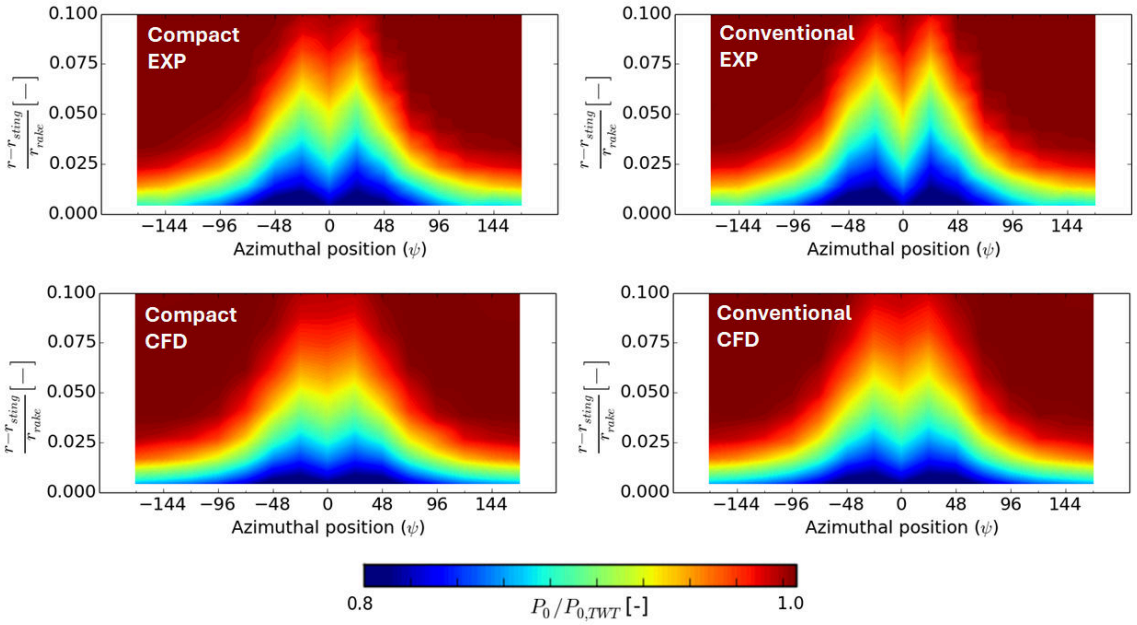
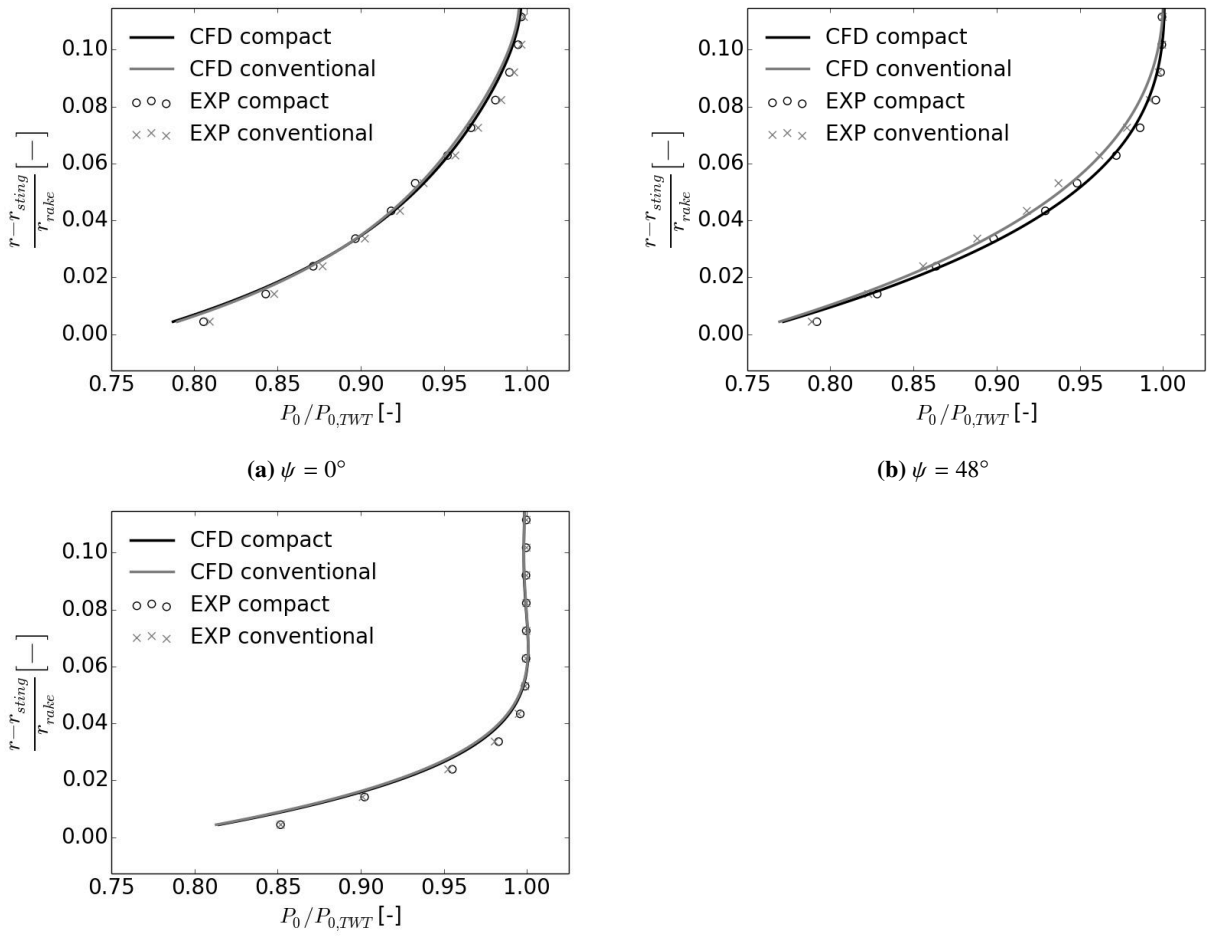


Fig. 8 Azimuthal changes of total pressure ratio at the rake location for mid-cruise conditions (M = 0.85, MFCR = 0.7 and $\alpha_{nac} = 4.5°$)

For this mid-cruise condition (M = 0.85, MFCR = 0.7 and $\alpha_{nac} = 4.5°$), the computed and measured nacelle drag coefficient for the conventional nacelle (L_{nac}/r_{hi} = 3.6) was C_D = 0.0403. Similar level agreement was found for the compact design (L_{nac}/r_{hi} = 3.1) with a nacelle drag coefficient of 0.0368 and 0.0369 for the numerical results and the measurements, respectively. As part of this work, the uncertainty of the measured nacelle drag was quantified. Referencing all uncertainty estimates to the conventional configuration as datum, the bias uncertainties were then differenced and the stochastic contributions summed by quadrature. This resulted in a measured drag reduction of the compact nacelle relative to the conventional of 8.5%, with experimental bias and stochastic components of +0.2% and ±1.2%, respectively. This drag coefficient reduction slightly increases to 8.8% for the CFD results. This demonstrates, for the first time, the measured nacelle drag coefficient reduction of HBPR compact nacelles relative to conventional designs. In addition, it shows that RANS CFD methods can predict the drag benefits expected from compact civil aero-engine nacelles, and verifies that the proposed multi-point, multi-objective optimization method has worked (Section III.A).

2. Sensitivity to Mach number

For both nacelles, i.e. compact (L_{nac}/r_{hi} = 3.1) and conventional (L_{nac}/r_{hi} = 3.6), the nacelle drag sensitivity to flight Mach number was investigated. For representative mid-cruise conditions with MFCR = 0.7 and $\alpha_{nac} = 4.5°$, Figure 10 shows the drag changes for free-stream Mach numbers between 0.78 and 0.86. Across this range, the drag coefficient predicted by CFD was typically within an average 2% of the experimental drag for both configurations, with



(a) ψ = 0°

(b) ψ = 48°

(c) ψ = 96°

Fig. 9 Boundary layer profiles at the rake location for selected azimuthal locations at mid-cruise conditions (M = 0.85, MFCR = 0.7 and α_{nac} = 4.5°)

a maximum difference of 4.2% at M = 0.8 for the compact nacelle.

Changes in flight Mach number can significantly affect the nacelle aerodynamics (Figure 11). For transonic conditions an increase in M usually results in a greater initial acceleration around the nacelle lip that increases the peak isentropic Mach number (M_{is}) along the nacelle. This is followed by a stronger pre-shock M_{is} and a downstream movement of the shock location. For a nominal mid-cruise MFCR = 0.7 and α_{nac} = 4.5°, Figure 11 shows the comparisons of isentropic Mach number between CFD and measurements for the five controlled aero-lines (ψ = 0°, 45°, 90°, 135° and 180°) of the compact aero-engine nacelle at M = 0.80, 0.85 and 0.86. Across the different Mach numbers and azimuthal locations there is an excellent agreement between CFD and experiments in terms of peak M_{is}, pre-shock M_{is} and shock-wave location. Based on the numerical simulations, and relative to the flight condition with M = 0.8, the peak M_{is} increases by approximately +0.05 and +0.06 on the top-line (ψ = 0°) when the Mach number increases to 0.85 and 0.86, respectively. There is also a change in the pre-shock Mach number of around +0.03 for M = 0.85 and

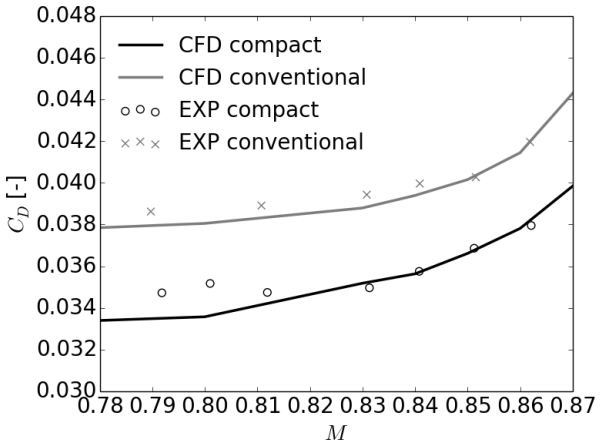


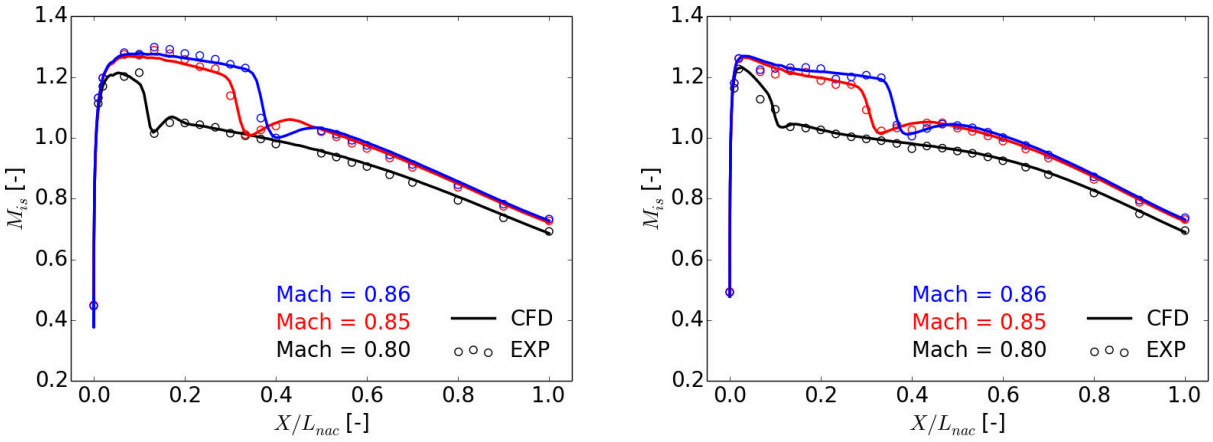
Fig. 10 Nacelle drag coefficient as a function of Mach number at fixed MFCR = 0.7 and α_{nac} = 4.5°

about +0.05 when M increases to 0.86 for this controlled aero-line. There are notable differences in the shock location across the different Mach number values, with positions of X/L_{nac} = 0.10, 0.30 and 0.35 at M = 0.80, 0.85 and 0.86, respectively (Figure 11). Although the comparisons for the conventional design are not presented in this work, the level of agreement between the numerical simulations and the experimental data was similar to the compact nacelle.

3. Sensitivity to massflow capture ratio

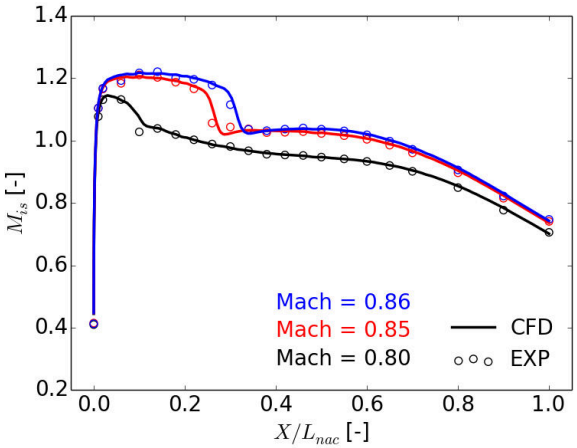
As the MFCR reduces, the stagnation point moves inside the inner intake aero-line. Therefore, there is a stronger initial acceleration around the nacelle lip which results in larger peak and pre-shock Mach numbers. As a consequence of the stronger shock-waves, the nacelle drag increases due to larger wave drag. The changes in the viscous term as a function of massflow capture ratio are 2 orders of magnitude lower than the pressure term. Compact civil aero-engine nacelles are more sensitive to changes in massflow capture ratio (MFCR) than conventional designs [16]. This is typically caused by the greater curvatures on the nacelle lip for compact designs, and the resulting flow accelerations that terminate in stronger shocks and a concomitant wave drag.

The nacelle drag characteristics of both nacelles are compared at fixed M = 0.84 and α_{nac} = 4.5° as a function of MFCR (Figure 12). For the compact nacelle, experimental data was gathered for a range of MFCR between 0.7 and 0.3, and MFCR = 0.7, 0.65 and 0.35 were measured for the conventional (Figure 6) . Across the range of considered MFCRs, the drag gradients are reasonably well predicted by the numerical simulations. For an aerodynamically challenging MFCR of 0.35, the numerical simulations overpredict by approximately 3.5% the nacelle drag for the L_{nac}/r_{hi} = 3.1 design. A similar overprediction was obtained for the L_{nac}/r_{hi} = 3.6 configuration (Figure 12). There is very good agreement in the overall sensitivity to MFCR for both nacelles. For example, between the cruise condition (MFCR = 0.7) and the low MFCR of 0.35, the experimental increase in drag is a factor of 3.0 and 1.8, for the compact and conventional nacelles, respectively. These are very considerable changes in the nacelle drag aerodynamics, which are

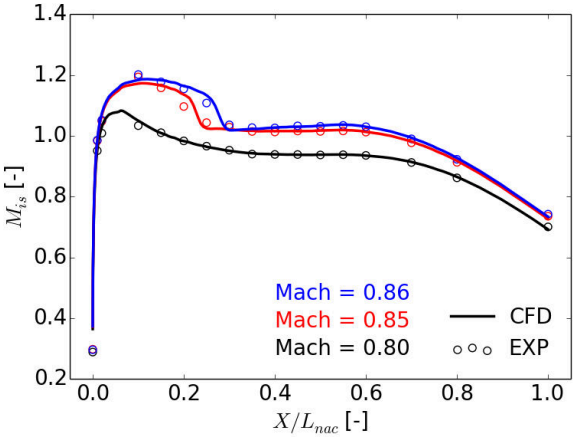


(a) $\psi = 0°$

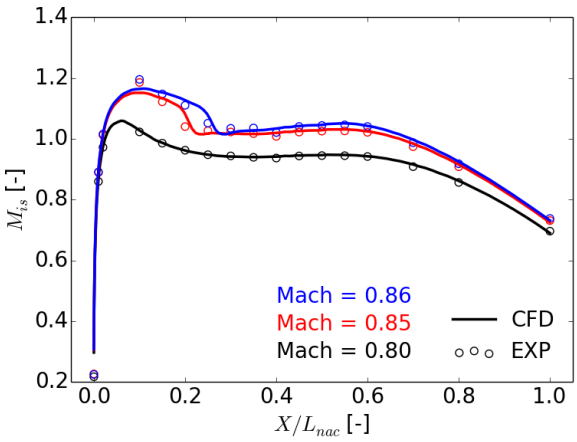
(b) $\psi = 45°$



(c) $\psi = 90°$



(d) $\psi = 135°$



(e) $\psi = 180°$

Fig. 11 Isentropic Mach number distribution along the compact nacelle (L_{nac}/r_{hi} = 3.1) as a function of Mach number at fixed MFCR = 0.7 and $\alpha_{nac} = 4.5°$

well predicted by CFD with increments of 3.1 and 1.9.

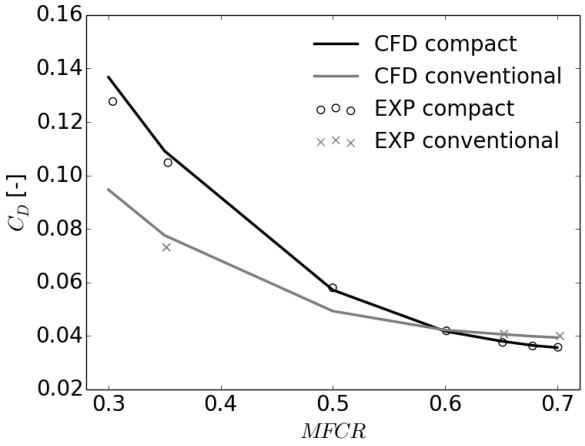
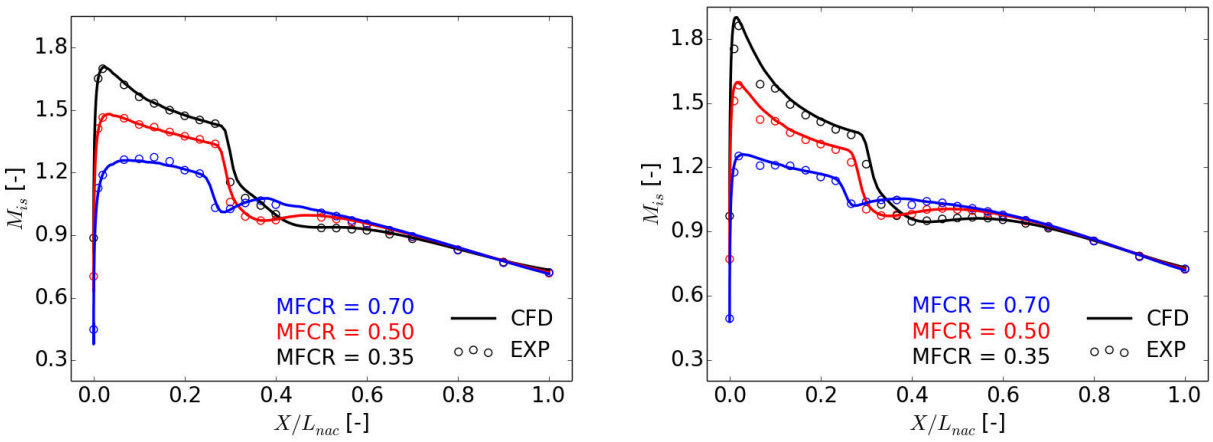
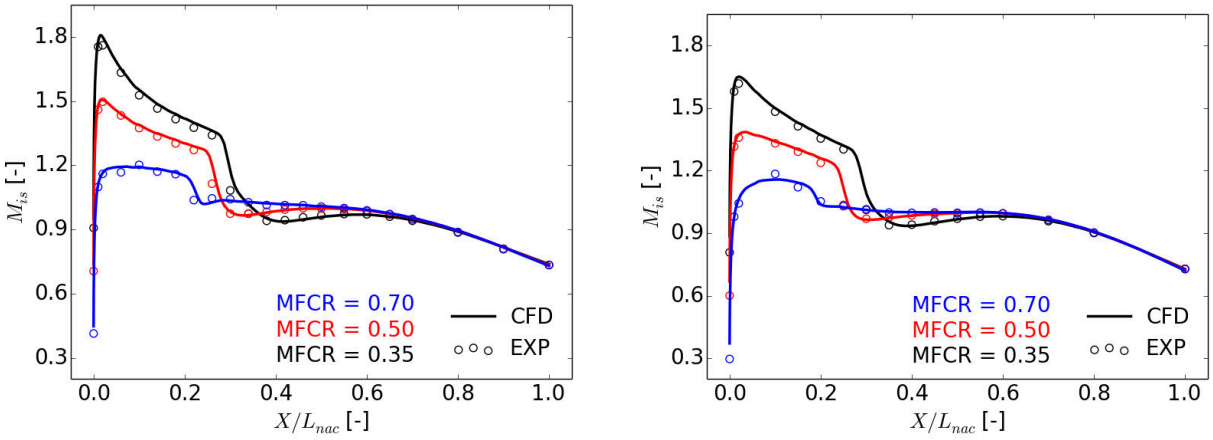


Fig. 12 Nacelle drag coefficient as a function of MFCR at fixed M = 0.84 and α_{nac} = 4.5°

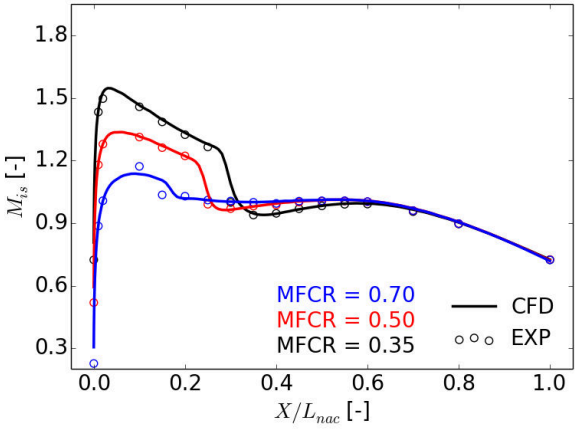
A change in the operating massflow capture ratio usually results in significant differences in the nacelle aerodynamics. As the MFCR reduces, the stagnation point moves further into the intake. This results in a larger acceleration around the nacelle lip with a significant increase in peak isentropic Mach number and pre-shock M_{is}. For a nominal M = 0.84 and α_{nac} = 4.5°, Figure 13 shows for the compact nacelle the comparison of isentropic Mach number for CFD and measurements along the five controlled aero-lines (ψ = 0°, 45°, 90°, 135° and 180°) at MFCR = 0.70, 0.50 and 0.35. The agreement between the numerical simulations and the experimental data is very good with peak isentropic Mach number within ΔM_{is} = 0.03, pre-shock M_{is} within ΔM_{is} = 0.02 and shock location within $\Delta X/L_{nac}$ = 0.04. Relative to a nominal MFCR = 0.7, the reduction of MFCR to 0.50 and 0.35 results in an increase in the measured peak M_{is} in the top aero-line (ψ = 0°) of ΔM_{is} = 0.25 and 0.47, respectively. For this aero-line, there are significant changes on the pre-shock Mach number as a function of massflow capture ratio. For the experimental data and relative to the condition with MFCR = 0.7, there is an increase of ΔM_{is} = +0.14 and +0.22 when the MFCR is reduced to 0.50 and 0.35, respectively. The CFD predicted the same changes in M_{is}. There is good agreement in the shock location in which the difference between CFD and measurements is within $\Delta X/L_{nac}$ = 0.01 for the top aero-line (ψ = 0°). There was a similar level of accuracy in terms of peak and pre-shock Mach number as well as shock location across the different aero-lines. Relative to the top aero-line (ψ = 0°), the peak isentropic Mach number is increases by ΔM_{is} = 0.25 at the top control aero-line (ψ = 45°). This was found for both CFD and measurements. This variation is caused by the lower nacelle initial radius of curvature of the nacelle at ψ = 45°, which has a large impact on the initial acceleration along the lip. The same agreement on the M_{is} distribution was obtained for the L_{nac}/r_{hi} = 3.6 nacelle across the range of massflow capture ratios.



(a) $\psi = 0°$ **(b)** $\psi = 45°$



(c) $\psi = 90°$ **(d)** $\psi = 135°$



(e) $\psi = 180°$

Fig. 13 Isentropic Mach number distribution along the compact nacelle (L_{nac}/r_{hi} = 3.1) as a function of MFCR at fixed M = 0.84 and $\alpha_{nac} = 4.5°$

4. Sensitivity to incidence angle

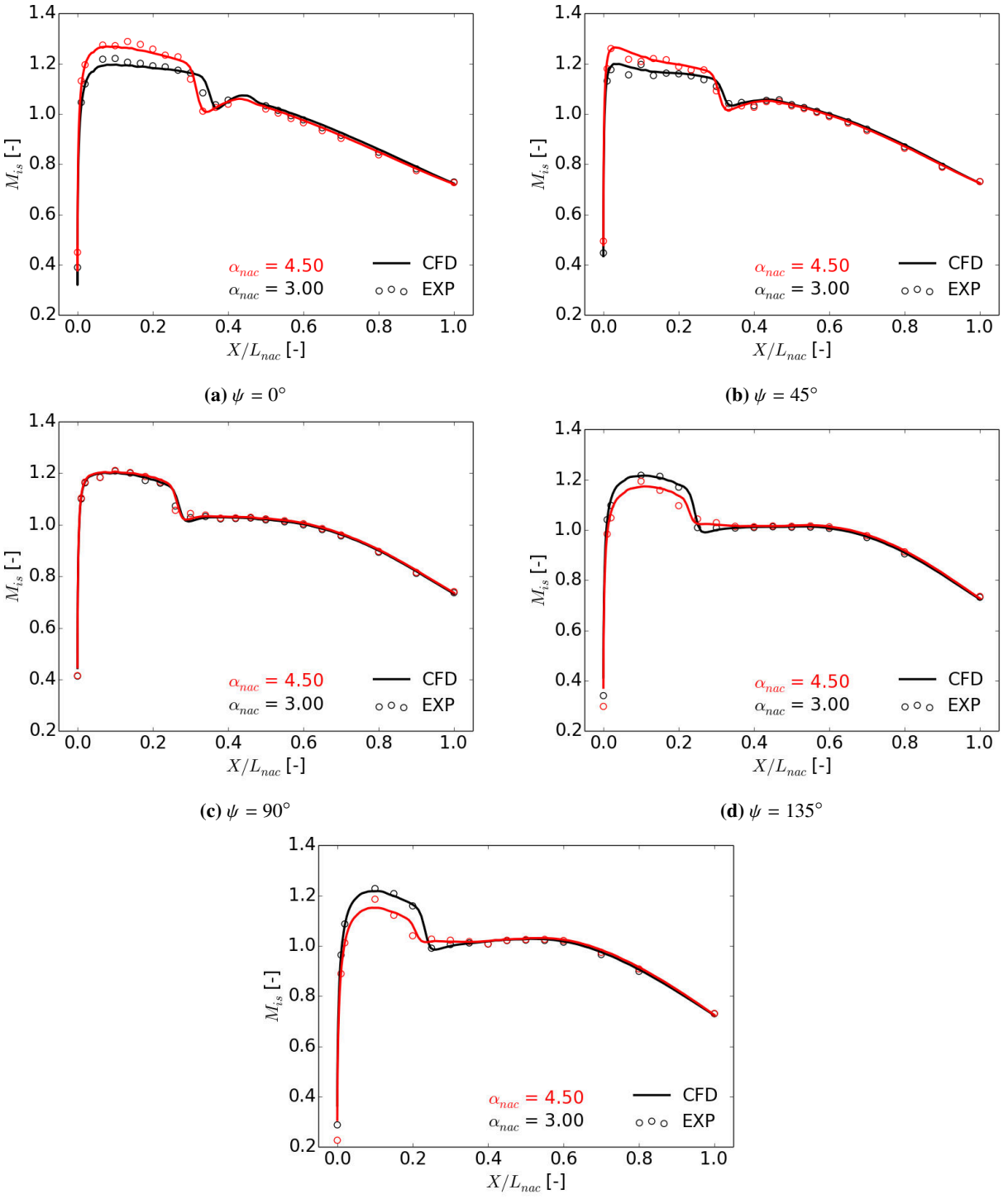
Other key parameter that has an impact on the nacelle drag and aerodynamic characteristics is the angle of attack. To provide an insight of how it affects the nacelle aerodynamics, the Mach number and massflow capture ratio were fixed to a nominal mid-cruise condition with M = 0.85 and MFCR = 0.7, and two angles of attack were considered, α_{nac} = 3° and 4.5° . For both configurations, the sensitivity of nacelle drag to changes in α_{nac} from 3° to 4.5° is modest. For the conventional nacelle, this is approximately 0.9% and 1.1% for the measurements and CFD, respectively. Similar sensitivity was identified for the compact nacelle with increments of 0.7% for both methods. These variations are within the experimental uncertainty.

Depending on the aero-line, a change in angle of attack has a different impact on the M_{is} distribution (Figure 14). For example, for the azimuthal locations of ψ = 0° and 45° the peak and pre-shock Mach number increases with the angle of attack due to the larger acceleration around the nacelle lip (Figures 14a and 14b). For the side aero-line with ψ = 90°, the M_{is} distribution along the fan cowl is similar for the different angles of attack (Figure 14c). Lastly, for ψ = 135° and ψ = 180° the acceleration around the nacelle lip decreases with the increase of α_{nac} which results in lower peak and pre-shock M_{is} (Figures 14d and 14e). As for previous comparisons (Sections III.C.2 and III.C.3), there is also a good agreement in the isentropic Mach number distribution for the different angles of attack considered. The key characteristics of peak M_{is} , pre-shock M_{is} and shock location are well predicted by CFD with errors within ΔM_{is} = 0.02, ΔM_{is} = 0.03 and $\Delta X/L_{nac}$ = 0.01, respectively. For the nacelle aero-lines of 0°, 45° and 90°, which has a large impact on the nacelle drag, the changes in isentropic Mach number as a function of angle of attack are modest. For example, the pre-shock Mach number increases by 0.03 in the top aero-line when the angle of attack changes from 3° to 4.5° . Therefore, the nacelle drag only increases by 0.7%.

IV. Conclusions

A combined numerical and experimental investigation was carried out to quantify the aerodynamic characteristics of civil large aero-engine nacelles. This included cruise conditions as well as the sensitivity to the key aerodynamic parameters of Mach number, massflow capture ratio and angle of attack. Across the range of operating points, CFD simulations were performed and the results have been compared with measurements in a transonic wind tunnel.

Two nacelles were designed with a multi-point, multi-objetive optimization method. These were representative of a conventional configuration and a compact design that is expected for future civil aero-engines. Both nacelles were studied in an industrial transonic wind tunnel where detailed measurements of the nacelle drag and its associated isentropic Mach number distributions were performed. For the first time in the literature, the aerodynamic benefits of compact nacelles relative to conventional is demonstrated through a detailed wind tunnel test campaign. The measured nacelle drag reduction of the compact nacelle was 8.5% at mid-cruise conditions. This was in agreement with CFD that predicted a reduction of 8.8%. These drag reductions are similar to those identified during the optimization process,



(a) $\psi = 0°$

(b) $\psi = 45°$

(c) $\psi = 90°$

(d) $\psi = 135°$

(e) $\psi = 180°$

Fig. 14 Isentropic Mach number distribution along the compact nacelle (L_{nac}/r_{hi} = 3.1) as a function of α_{nac} at fixed M = 0.85 and MFCR = 0.7

which establishes confidence in the proposed design approach that is usually used within an industrial context. Across a wide range of operating conditions with different Mach numbers (M) and massflow capture ratios (MFCRs), the predicted nacelle drag was typically within approximately 2% of the measurements at a representative incidence angle (α_{nac}) of 4.5°. Large changes in the nacelle drag were measured when the MFCR was reduced from 0.7 to 0.35 at fixed M = 0.84 and α_{nac} = 4.5°. For the compact nacelle, the drag increased by a factor of 3.0. This was successfully predicted by CFD with an increment of 3.1. The capability of the computational approach has been also demonstrated for the accurate prediction of the associated nacelle aerodynamic characteristics in terms of peak and pre-shock isentropic Mach number and shock location. The main contribution of this work is the validation of the nacelle design and optimization method, and the quantification of nacelle drag reduction for new compact designs with both numerical and experimental methods. Overall, the potential impact of this is in the development of more fuel efficient aircraft.

Funding Sources

This project has received funding from the Clean Sky 2 Joint Undertaking (JU) under grant agreement number 101007598. The JU receives support from the European Union's Horizon 2020 research and innovation programme and the Clean Sky 2 JU members other than the Union.

Data availability statement

Due to commercial confidentiality agreements the supporting data are not available.

References

[1] Arnaldo-Valdes, R. M., Burmaoglu, S., Tucci, V., da Costa, C. B., Luiz, M., Mattera, L., Gomez, C., and Victor, F., "Flight Path 2050 and ACARE Goals for Maintaining and Extending Industrial Leadership in Aviation: A Map of the Aviation Technology Space," *Sustainability*, Vol. 11, No. 7, 2019.

[2] Ranasinghe, K., Guan, K., Gardi, A., and Sabatini, R., "Review of Advanced Low-Emission Technologies for Sustainable Aviation," *Energy*, Vol. 188, 2019, p. 115945.

[3] Undavalli, V., Olatunde, O., Boylu, R., Wei, C., Haeker, J., Hamilton, J., and Khandelwal, B., "Recent Advancements in Sustainable Aviation Fuels," *Progress in Aerospace Sciences*, Vol. 136, 2023, p. 100876.

[4] Adler, E., and Martins, J., "Blended Wing Body Configuration for Hydrogen-Powered Aviation," *Journal of Aircraft*, Vol. 61, No. 3, 2024, pp. 887–901.

[5] Scholz, A., Michelmann, J., and Hornung, M., "Fuel Cell Hybrid-Electric Aircraft: Design, Operational, and Environmental Impact," *Journal of Aircraft*, Vol. 60, No. 3, 2023, pp. 606–622.

[6] Lukaczyk, T., Wendorff, A. D., Colonno, M., Economon, T., Alonso, J., Orra, T., and Ilario, C., "SUAVE: An Open-Source

Environment for Multi-Fidelity Conceptual Vehicle Design," *16th AIAA/ISSMO Multidisciplinary Analysis and Optimization Conference, AIAA Paper 2015-3087*, 2015.

[7] Daggett, D., Brown, S., and Kawat, R., "Ultra-Efficient Engine Diameter Study," Tech. Rep. CR-2003-212309, NASA, 2003.

[8] Ahuja, J., and Mavris, S. A. R. D., "Sensitivity Analysis of the Overwing Nacelle Design Space," *Journal of Aircraft*, Vol. 59, No. 6, 2022, pp. 1478–1492.

[9] Tejero, F., MacManus, D., Goulos, I., and Sheaf, C., "Propulsion Integration Study of Civil Aero-Engine Nacelles," *The Aeronautical Journal*, Vol. 128, No. 1320, 2023, pp. 325–339.

[10] Daggett, D., "Ultra-Efficient Engine Technology Systems Integration and Environmental Assessment," Tech. Rep. CR-2002-211754, NASA, 2002.

[11] Peters, A., Spakovszky, Z. S., Lord, W., and Rose, B., "Ultrashort Nacelles for Low Fan Pressure Ratio Propulsors," *Journal of Turbomachinery*, Vol. 137, No. 2, 2015.

[12] Birch, N., "2020 Vision: The Prospects for Large Civil Aircraft Propulsion," *The Aeronautical Journal*, Vol. 104 (1038), 2000, pp. 347–352.

[13] Tejero, F., MacManus, D., Heidebrecht, A., and Sheaf, C., "Artificial Neural Network for Preliminary Design and Optimisation of Civil Aero-engine Nacelles," *The Aeronautical Journal*, 2024, p. 1–20.

[14] Hueso-Rebassa, J., MacManus, D., Tejero, F., Goulos, I., Sánchez-Moreno, F., and Sheaf, C., "Design Optimisation of Non-Axisymmetric Exhausts for Installed Civil Aero-Engines," *Aerospace Science and Technology*, Vol. 142, 2023, p. 108700.

[15] Tejero, F., Robinson, M., MacManus, D., and Sheaf, C., "Multi-Objective Optimization of Short Nacelles for High Bypass Ratio Engines," *Aerospace Science and Technology*, Vol. 91, 2019, pp. 410–421.

[16] Boscagli, L., MacManus, D., Tejero, F., Sabnis, K., Babinsky, H., and Sheaf, C., "Characteristics of Shock-Induced Boundary-Layer Separation on Nacelles Under Windmilling Diversion Conditions," *AIAA Journal*, Vol. 62, No. 1, 2024, pp. 79–91.

[17] Goulos, I., MacManus, D., Hueso-Rebassa, J., Tejero, F., Au, A., and Sheaf, C., "Impact of Installation on the Performance of an Aero-Engine Exhaust at Wind-Milling Flow Conditions," *Journal of Engineering for Gas Turbines and Power*, Vol. 146, No. 8, 2024, p. 081002.

[18] Goulos, I., Otter, J., Tejero, F., Rebassa, J. H., and MacManus, D., "Civil Turbofan Propulsion Aerodynamics: Thrust-Drag Accounting and Impact of Engine Installation Position," *Aerospace Science and Technology*, Vol. 111, 2020, p. 106533.

[19] Silva, V. T., Lundbladh, A., Xisto, C., and Grönstedt, T., "Over-wing Integration of Ultra-High Bypass Ratio Engines: A Coupled Wing Redesign and Engine Position Study," *Aerospace Science and Technology*, Vol. 138, 2023, p. 108350.

[20] Ahuja, J., Lee, C. H., Perron, C., and Mavris, D. N., "Comparison of Overwing and Underwing Nacelle Aeropropulsion Optimization for Subsonic Transport Aircraft," *Journal of Aircraft*, Vol. 61, No. 2, 2024, pp. 638–653.

[21] Swarthout, A., MacManus, D., Tejero, F., Matesanz-Garcia, J., Boscagli, L., and Sheaf, C., "A Comparative Assessment of Multi-Objetive Optimisation Methodologies for Aero-Engine Nacelles," *33rd Congress of the International Council of the Aeronautical Sciences: ICAS 2022*, 2022.

[22] Silva, V. T., Lundbladh, A., Petit, O., and Xisto, C., "Multipoint Aerodynamic Design of Ultrashort Nacelles for Ultrahigh-Bypass-Ratio Engines," *Journal of Propulsion and Power*, Vol. 38, No. 4, 2022, pp. 1–18.

[23] Tao, G., w. Wang, Ye, Z., Wang, Y., Luo, J., and Cui, J., "Multi-Fidelity and Multi-Objective Aerodynamic Short Nacelle Shape Optimisation under Different Flight Conditions," *The Aeronautical Journal*, Vol. 128, No. 1321, 2024, p. 517–546.

[24] Yildirim, A., Gray, J. S., Mader, C. A., and Martins, J. R., "Coupled Aeropropulsive Design Optimization of a Podded Electric Propulsor," *AIAA AVIATION 2021, AIAA Paper 2021-3032*, 2021.

[25] Yan, C., Zhang, Y., and Zhang, M., "Numerical Optimization of Transonic Natural Laminar Flow Nacelles," *Chinese Journal of Aeronautics*, Vol. 36, No. 6, 2023, pp. 35–51.

[26] Magrini, A., Buosi, D., and Benini, E., "Analysis of Installation Aerodynamics and Comparison of Optimised Configuration of an Ultra-High Bypass Ratio Turbofan Nacelle," *Aerospace Science and Technology*, Vol. 128, 2022, p. 107756.

[27] Lei, R., Bai, J., and Xu, D., "Aerodynamic Optimization of Civil Aircraft with Wing-Mounted Engine Jet Based on Adjoint Method," *Aerospace Science and Technology*, Vol. 93, 2019, p. 105285.

[28] Langley, M., "The Design of Axisymmetric Cowls for Podded Nacelles for High Bypass Ratio Turbofan Engines," Tech. Rep. 3846, Aeronautical Research Council, 1979.

[29] Robinson, M., MacManus, D., and Sheaf, C., "Aspects of Aero-Engine Nacelle Drag," *Proceedings of the Institution of Mechanical Engineers, Part G: Journal of Aerospace Engineering*, Vol. 233, No. 5, 2018, pp. 1667–1682.

[30] Green, J., Weeks, D., and Brooma, J., "ARC RM 3791: Prediction of Turbulent Boundary Layers and Wakes in Compressible Flow by a Lag-Entrainment Method," Tech. rep., HMSO for Aeronautical Research Council, MoD, 1977.

[31] Meyn, L., "An Uncertainty Propagation Methodology That Simplifies Uncertainty Analyses," *38th Aerospace Sciences Meeting and Exhibit, AIAA Paper 2000-0149*, 2000.

[32] Cahill, D., "Assessment of Experimental Uncertainty with Application to Wind Tunnel Testing," *AIAA Standard AIAA S-071A-1999, Rev A.*, 1999.

[33] The American Society of Mechanical Engineers, *MFC-26-2011 - Measurement of Gas Flow by Bellmouth Inlet Flowmeters*, ASME, 2011.

[34] AGARDograph AG-237, "Guide to In-Flight Thrust Measurement of Turbojets and Fan Engines," Tech. rep., AGARD Report, 1979.

[35] Deb, K., Pratap, A., Agarwal, S., and Meyarivan, T., "A Fast and Elitist Multiobjective Genetic Algorithm: NSGA-II," *IEEE Transactions on Evolutionary Computation*, Vol. 6, (2), 2002, pp. 182 – 197.

[36] *ANSYS FLUENT User's Guide*, Ansys Inc., 275 Technology Drive, Canonsburg, PA 15317, ????

[37] Sutherland, W., "The Viscosity of Gases and Molecur Force," *Philosophical Magazine*, Vol. 5, No. 35, 1893, pp. 507–531.

[38] Roache, P., "A Method for Uniform Reporting of Grid Refinement Studies," *Journal of Fluids Engineering*, Vol. 116 (3), 1994, pp. 405–413.

[39] Jones, B., *Measurement of Profile Drag by the Pitot-Traverse Method*, ARC R & M 1688, 1936.

[40] Geyr, H., and Rossow, C., "A Correct Thrust Determination Method for Turbine Powered Simulators in Wind Tunnel Testing," *41st AIAA/ASME/SAE/ASEE Joint Propulsion Conference Exhibit, AIAA Paper 2005-3707*, 2005.

[41] Barlow, J. B., Rae, W. H., and Pope, A., *Low Speed Wind Tunnel Testing*, 3rd ed., John Wiley and Sons, Hoboken, 1999.

[42] Carr, A. M., "Estimation of Windmilling Drag and Airflow of Tubo-Jet and Turbo-Fan Engines," Tech. Rep. ESDU-81009, ESDU, November 1981.

[43] Li, J., and Zhang, M., "Adjoint-Free Aerodynamic Shape Optimization of the Common Research Model Wing," *AIAA Journal*, Vol. 59, 2021, p. 1990–2000.



https://dspace.org/

Aerodynamics of high-bypass-ratio aeroengine nacelles: numerical and experimental investigation

Tejero, Fernando; MacManus, David G.; Sánchez-Moreno, Francisco; Schreiner, B. Deneys J.; Hill, Andrea ...

2025-07
American Institute of Aeronautics and Astronautics (AIAA)
https://doi.org/10.2514/1.c038164
Tejero F, MacManus D, Sanchez-Moreno F, et al., (2025) Aerodynamics of high-bypass-ratio aeroengine nacelles: numerical and experimental investigation. Journal of Aircraft, Volume 62, Issue 4, July 2025, pp. 1004-1017

Downloaded from a DSpace repository. https://dspace.org/